This is the peer-reviewed, final accepted version for American Mineralogist, published by the Mineralogical Society of America.
The published version is subject to change. Cite as Authors (Year) Title. American Mineralogist, in press.
DOI: https://doi.org/10.2138/am-2022-8588. http://www.minsocam.org/

Revision 1

Revision of the $CaMgSi_2O_6$–CO_2 *P-T* phase diagram at 3-6 GPa

Anton Shatskiy[1*], Yulia G. Vinogradova[1], Anton V. Arefiev[1], Konstantin D. Litasov[2]

[1]Vernadsky Institute of Geochemistry and Analytical Chemistry of the Russian Academy of Science, Moscow 119991, Russia

[2]Vereshchagin Institute for High Pressure Physics of the Russian Academy of Science, Troitsk, Moscow, 108840, Russia

*telephone: +7 (913) 385 6129, e-mail: shatskiy@geokhi.ru

Abstract

In the present work, we reexamined the phase relationships in the system diopside–CO_2 in the range of 3-6 GPa and 850-1500 °C in multianvil experiments including reversal ones lasting up to 169 hours. The reaction $CaMgSi_2O_6$ (clinopyroxene) + $2CO_2$ (fluid) = $2SiO_2$ (quartz/coesite) + $CaMg(CO_3)_2$ (dolomite) passes through 3 GPa/950 °C with a slope of 6 MPa/°C and terminates at an invariant point near 4.5 GPa/1200 °C, where carbonate liquid coexists with clinopyroxene, coesite, dolomite and CO_2 fluid. The newly determined boundary has the equation P(GPa) = 0.006×T(°C) – 2.7. As temperature increases to 1250 °C at 4.5 GPa, liquid, dolomite, and coesite disappear and clinopyroxene coexists with CO_2 fluid. As pressure increases to 6 GPa, the solidus temperature increases to 1300 °C revealing a slope of 15 MPa/°C. At 4.5 and 6 GPa, solidus melts contain about 1 wt% SiO_2. As temperature increases to 1400 and 1500 °C at 6 GPa, the silica contents in the carbonate melt increase to 6 and 13 wt%, respectively. Our data combined with that of Luth (2006)

indicates that above 4.5 GPa the liquidus reaction involving clinopyroxene and CO_2 sweeps down through 350 °C via a pressure maximum near 5.3 GPa to meet the invariant point at 4.5 GPa. The shape of the diopside-CO_2 solidus resembles that of lherzolite–CO_2 (Wyllie and Huang 1975) but shifted by 2 GPa to higher pressure. Thus, the deep depression along the solidi in the system CaO–MgO–SiO_2–CO_2 is a fundamental feature of both ultramafic and mafic assemblages at depths of 70-150 km.

Keywords: CO_2 fluid, carbonation, clinopyroxene, phase relations, high pressure, multianvil experiments, Earth's mantle

Nomenclature			
Ca#	100·Ca/(Ca+Mg)	F	fluid
Cal	calcite	Fo	forsterite
Coe	coesite	Gr	graphite
Cpx	clinopyroxene	L	liquid
Di	diopside	Mgs	magnesite
Dia	diamond	Ol	olivine
Dol	dolomite	Opx	orthopyroxene
		Qz	quartz

Introduction

The relative stability of the CO_2 fluid, carbonates, and their melts, controlled by the reactions of carbonation-decarbonation and melting, are of key importance for the understanding genesis of CO_2-rich magmas (kimberlites, carbonatites), diamond-forming fluids, and the deep carbon cycle. The system CaO–MgO–SiO_2–CO_2 (CMS-CO_2) is a basis for studying these reactions (Wyllie and Huang 1975b). The carbonation of peridotites in the CMS-CO_2 system is controlled by the reaction,

$$2Mg_2SiO_4\ (Ol) + CaMgSi_2O_6\ (Cpx) + 2CO_2\ (F) = 2Mg_2Si_2O_6\ (Opx) + CaMg(CO_3)_2\ (Dol), \quad (1)$$

which lowers the solidus from 1600 to 1200 °C at 2.5 GPa (Wyllie and Huang 1975a) (Fig. 1). Solidus ledges are observed not only for the model CMS-CO_2 system but are specific for complex peridotite-CO_2 systems (Wallace and Green 1988; Falloon and Green 1989).

In a mafic suit modeled by the CMS-CO_2 system, the carbonation reaction,

$$CaMgSi_2O_6\ (Cpx) + 2CO_2\ (F) = 2SiO_2\ (Qz/Coe) + CaMg(CO_3)_2\ (Dol), \quad (2)$$

occurs 1.5-2 GPa higher (Wyllie et al. 1983; Luth 1995; 2006) (Fig. 1). However, the effect of carbonation on the mafic suit solidus remains unclear. The solidus ledge in the carbonate-bearing mafic system has been detected by Hammouda (2003) for the eclogite-CO_2 system. He found a significant drop (by ~250 °C) in the solidus temperature at ~ 6 GPa. Based on the study (Luth 2006), no solidus drop occurs at pressures above the carbonation reaction in the $CaMgSi_2O_6$-CO_2 system (Fig. 1). Yet, following the experiments by (Luth 1995; 2006), reaction 2 stabilizes dolomite at temperatures 150-200 °C higher than dolomite melting reported by (Buob et al. 2006; Müller et al. 2017; Shatskiy et al. 2018) (Fig. 2). To clarify this discrepancy, additional experiments in the $CaMgSi_2O_6$-CO_2 system at 4.5–6 GPa are needed.

In all previous works, the reaction was investigated only from the side of decarbonation in the experiments with a duration of 24 h and less (Fig. 2), which might be insufficient to achieve equilibrium at temperatures 800-1000 °C. Therefore, reverse experiments on diopside carbonation are needed to resolve this uncertainty.

We present new data on phase relations in the $CaMgSi_2O_6$–CO_2 system at 3-6 GPa. To clarify the issues mentioned above we studied both carbonation and decarbonation reactions at 3 GPa in longer experiments (up to 169 h) and reexamined phase relations at 4.5 and 6 GPa to clarify the position of solidus in the $CaMgSi_2O_6$-CO_2 system.

Experimental procedure

Synthetic diopside, reagent grade SiO_2, $Ag_2C_2O_4$, $CaCO_3$, and natural magnesite (< 0.1% impurity) from Brumado (Bahia, Brazil) were employed as components of starting mixtures. Two starting compositions were prepared. The first one is carbonate-silica mixture: $CaCO_3 + MgCO_3 + 2SiO_2$, corresponding to $CaMgSi_2O_6 + 2CO_2$. The mixture was prepared by blending starting powders with alcohol in an agate mortar. The prepared mixtures were dried at 300 °C for 1 h and then stored at 150 °C until use. The second starting composition, $4CaMgSi_2O_6 + Ag_2C_2O_4$, was prepared by layer-by-layer loading where diopside and oxalate powders were placed as multiple layers (Fig. 3a). The ratio of components in the second starting composition is approximate. The second starting material was not blended and dried to avoid the decomposition of the silver oxalate. Besides, in one run, the mixture $CaCO_3 + MgCO_3 + SiO_2$, corresponding to $1/2CaMgSi_2O_6 + 1/2CaMg(CO_3)_2 + CO_2$ was employed.

Experiments were conducted using graphite capsules. We also performed one experiment using both graphite and platinum capsules to verify if there was any effect of capsule material on the results. The experiments were run in a multianvil 1500-ton DIA-type press 'Discoverer'. The experimental procedure is identical to that described earlier by (Shatskiy et al. 2021).

The temperature was measured using a W97Re3-W75Re25 thermocouple. No correction of the pressure effect on the electromotive force was applied. During the experiment, the sample temperature was controlled automatically in a thermocouple mode within 2 °C of the set value. The temperature distribution in the cell was examined using thermal modeling software (Hernlund et al. 2006). The results of modeling were also verified experimentally (Shatskiy et al. 2013) using a two-pyroxene thermometer (Brey and Kohler, 1990). The maximum temperature gradients within individual samples and across the sample charge vary from 4 to 8 °C/mm as temperature increases from 800 to 1300 °C, respectively (Podborodnikov et al. 2019). The modeling reveals that the maximum temperature difference between the thermocouple junction and samples is < 25 °C (Shatskiy et al.

2022). Pressure calibration was performed at room temperature by monitoring the resistance changes in Bi and Ba and at high temperatures using known phase transitions in SiO_2 and $CaGeO_3$ (Shatskiy et al. 2018). Uncertainty in the temperature and pressure measurements in the present study are estimated to be < 25 °C and < 0.5 GPa, respectively.

Samples were studied using a MIRA 3 LMU scanning electron microscope (Tescan Orsay Holding, Brno-Kohoutovice, Czech Republic), coupled with an INCA energy-dispersive X-ray microanalysis system 450, equipped with the liquid nitrogen-free Large area EDX X-Max-80 Silicon Drift Detector (Oxford Instruments Nanoanalysis Ltd., High Wycombe, UK) (Lavrent'ev et al. 2015). Energy-dispersive X-ray spectra (EDS) were collected by using an electron beam-rastering method, in which the stage is stationary while the electron beam moves over the surface area, with dimensions 3–10 μm (for silicate minerals) and 20–100 μm (for a quenched melt) at 20 kV accelerating voltage and 1.5 nA beam current. The live counting time for X-ray spectra was 20 s. The silicon drift detector energy-dispersive X-ray spectrometry (SDD-EDS) enables accuracy and precision equivalent to that of WDS in the case of routine analysis of rock-forming silicate minerals (Lavrent'ev et al. 2015; Newbury and Ritchie 2015).

Silica polymorphs were identified using a Horiba Jobin Yvon LabRAM HR800 Raman microspectrometer equipped with a multi-channel LN/CCD detector with a resolution of 1024 pixels and 532.1 nm solid-state laser.

Experimental results

Experiment at 6 GPa, 1100 °C in the Pt and graphite capsules

In the experiment at 1100 °C (D238, 147 h), the starting assemblies $CaCO_3 + MgCO_3 + 2SiO_2$ and $4CaMgSi_2O_6 + Ag_2C_2O_4$ in Pt capsules and $CaCO_3 + MgCO_3 + 2SiO_2$ in graphite capsule were simultaneously loaded. The cross-sections of the samples are shown in Fig. 3. In the starting assembly

114 $4CaMgSi_2O_6 + Ag_2C_2O_4$, the original oxalate layers were converted into thin layers of silver
115 surrounded by a newly formed layer of coesite-dolomite aggregate (Fig. 3a, b). Coesite forms
116 isometric euhedral crystals 3-5 μm in size embedded in a dolomite matrix. Among the crystals of
117 dolomite (Ca# 50) minor amounts of magnesite (Ca# 5) and aragonite (Ca# 100) crystals < 5 μm in
118 size appear (Fig. 3b, Table 1). The appearance of minor amounts of magnesite and aragonite is due to
119 the proximity of the reaction boundary $MgCO_3$ (Mgs) + $CaCO_3$ (Arg) = $CaMg(CO_3)_2$ (Dol) (Luth
120 2001). The newly formed layers are sandwiched by layers of clinopyroxene (stoichiometric diopside)
121 with a grain size of 10-30 μm (Fig. 3a). The presence of clinopyroxene is consistent with its initial
122 excess in the $4CaMgSi_2O_6 + Ag_2C_2O_4$ starting composition. In the $CaCO_3 + MgCO_3 + 2SiO_2$ starting
123 mixture in both Pt and graphite capsules, the samples are represented by a homogeneous aggregate of
124 dolomite and coesite with minor amounts of magnesite and aragonite, like that in the newly formed
125 layers in the starting composition with oxalate (Fig. 3c-f). In the sample in the graphite capsule, a
126 grain of clinopyroxene 4×6 μm in size was observed (Table 1). The similarity of the obtained results
127 allows us to conclude that for the studied starting compositions, the capsule material, platinum or
128 graphite, does not have a decisive effect on the phase relationships.
129
130 **Experiments with the $CaCO_3 + MgCO_3 + 2SiO_2$ mixture at 6 GPa**
131 At 1300 °C (D225, 21 h), approximately half of the sample from the low-temperature (LT) side
132 is represented by an aggregate of coesite and dolomite (Fig. 4a, Table 1). Dolomite and coesite appear
133 as isometric euhedral to subhedral grains with sizes of 10-15 μm and 2-5 μm, respectively (Fig. 4b).
134 The sample also contains a minor amount of short prismatic crystals of clinopyroxene 2-5 μm in size
135 (Fig. 4b). The other half of the sample, from the high-temperature (HT) side, consists of isometric
136 euhedral coesite crystals, up to 50 μm in size, and products of quenched carbonate melt, represented

This is the peer-reviewed, final accepted version for American Mineralogist, published by the Mineralogical Society of America.
The published version is subject to change. Cite as Authors (Year) Title. American Mineralogist, in press.
DOI: https://doi.org/10.2138/am-2022-8588. http://www.minsocam.org/

by fibrous crystals of dolomite and containing clinopyroxene needles (Fig. 4a, c). The melt has Ca# 58 and contains 0.7 wt% SiO_2 (0.6 mol%) (Table 1).

At 1400 °C (D221, 9 h), the sample mainly consists of coesite and quenched carbonate melt. The melt forms a separate pool adjacent to the HT side of the capsule. The quenched melt consists of dolomite and minor clinopyroxene (Fig. 4d). The melt has Ca# 54 and contains 6 wt% SiO_2 (5 mol%) (Table 1). Most of the sample consists of isometric euhedral coesite crystals with a size varying from 5 to 80 μm and interstitial melt. A narrow (40 μm) lens of an aggregate of isometric crystals of magnesite (Ca# 10) (5-15 μm in size), coesite (5-8 μm in size), and clinopyroxene (Ca# 41) (3-5 μm in size) adjoin the LT capsule end (Fig. 4d, e).

At 1500 °C (D222, 4 h), the sample consists of quenched melt and coesite which forms well-shaped short-prismatic crystals, up to 100 μm in size, at the LT sample side. The quenched melt consists of a dendritic aggregate of dolomite and clinopyroxene (Fig. 4f). The melt has Ca# 48 and contains 13 wt% SiO_2 (10 mol%) (Table 1). Graphite flakes, 4-8 μm in size, are present in the melt at the boundary with the graphite capsule. Given the low solubility of elemental carbon in carbonate melt, 0.3 wt% at 6.8 GPa and 1700 °C (Sokol et al. 1998) and the spatial confinement of graphite flakes to the walls of the capsule, we believe that the observed graphite is not a product of melt quenching, but was formed during the experiment as a result of recrystallization of the graphite of the capsule.

Experiments with the $CaCO_3$ + $MgCO_3$ + $2SiO_2$ mixture at 4.5 GPa

At 1000 (run D234, 115 h) and 1100 °C (runs D226, 35 h and D233, 73 h), the samples are represented by a homogeneous aggregate of euhedral to subhedral crystals of coesite and dolomite, with a minor amount of clinopyroxene. The phases form isometric euhedral to subhedral grains with

160 a size of up to 5-10 μm (Fig. 5a). The apparent amount of clinopyroxene does not change when the
161 duration of the experiment is doubled (Table 1).

162 At 1200 °C (run D248, 25 h), the sample is predominantly represented by a homogeneous
163 aggregate of clinopyroxene crystals and a quenched carbonate melt filling the interstitial space
164 between clinopyroxene crystals (Fig. 5b). The melt contains numerous graphite flakes (Fig. 5d). The
165 quenched melt forms a fine aggregate of dolomite crystals and contains 1.4 wt% SiO_2 (1.1 mol%) and
166 has Ca# 64 (Table 2). Clinopyroxene has Ca# 45 and grows to isometric euhedral crystals, 10-15 μm
167 in size (Fig. 5d, Table 2). A lens of an aggregate of coesite and dolomite (Ca# 60) adjoins the LT end
168 of the capsule (Fig. 5b, c).

169 As temperature increases to 1250 °C (run D219, 24 h), carbonate melt, coesite, and dolomite
170 disappear and the sample is represented by a homogeneous aggregate of isometric clinopyroxene
171 grains, 5-10 μm in diameter, and graphite flakes (Fig. 5e, f).

172

173 **Carbonation and decarbonation at 3 GPa**

174 In the carbonation experiments conducted at 850 (run D254, 169 h) and 900 °C (run D312, 150
175 h) with the $4CaMgSi_2O_6 + Ag_2C_2O_4$ sandwiches in graphite capsules, the dolomite-coesite aggregate
176 appears at the interface between Ag metal and clinopyroxene (Fig. 6a, b). Unlike that, in the same
177 starting composition at 1000 °C (run D249, 118 h) only a minor amount of quartz and dolomite was
178 formed (Fig. 6c, d, Table 3).

179 In the decarbonation experiment at 1000 °C and duration of 87 h (run D228) in the $CaCO_3$ +
180 $MgCO_3 + 2SiO_2$ starting mixture, the sample mainly consists of dolomite-quartz aggregate, which
181 also contains newly formed clinopyroxene crystals with irregular shape (Fig. 6e, f, Table 3).
182 Clinopyroxene crystals grow at the interface between dolomite and quartz grains (Fig. 6g). The
183 distribution of clinopyroxene crystals in the sample volume is inhomogeneous. The crystals are

concentrated along the walls of the graphite capsule, while the center part contains a lesser amount of clinopyroxene (Fig. 6e, f, Table 3). The formation of coesite at 900 °C and quartz at 1000 °C, identified by Raman spectroscopy, is consistent with the position of the quartz-coesite transition reported by (Hemingway et al. 1998) (Fig. 7).

It was also found that when the duration is doubled at 1000 °C in the $CaCO_3 + MgCO_3 + 2SiO_2$ starting mixture (run D205, 163 h), the sample is almost completely converted to clinopyroxene (Fig. 6h, Table 3). The sample looks shrank and contains many voids (Fig. 6h), which indirectly indicate the presence of CO_2 fluid during the experiment. Clinopyroxene forms subhedral prismatic crystals 10-30 μm in size (Fig. 6i). The sample also contains a small amount of Mg-bearing calcite and quartz separated by clinopyroxene crystals (Fig. 6j, Table 3).

As the temperature increases to 1100 °C (run D207, 77 h), the $CaCO_3 + MgCO_3 + SiO_2$ starting mixture transforms to clinopyroxene-orthopyroxene-dolomite aggregate with numerous voids of presumably CO_2 fluid with irregular outlines (Fig. 6k, l, Table 3). Clinopyroxene grows to isometric euhedral crystals up to 15 μm in size, whereas dolomite forms subhedral isometric grains up to 30 μm in diameter (Fig. 6l). Ca# of clinopyroxene and dolomite differ from 50. Clinopyroxene is more magnesian with Ca# 44, while dolomite is more Ca-rich with Ca# 68 (Table 3). The sample also contains numerous graphite flakes, which are mainly concentrated in voids in the LT sample part, whereas its HT part is almost free of graphite (Fig. 6k l). This can be explained by the recrystallization of graphite of the capsule from the HT to LT side via CO_2 fluid driven by the graphite solubility difference in CO_2 fluid at a high and lower temperature.

Discussion

Comparison with previous data

The experimental results obtained are plotted in the *P-T* space in Figure 7. The formation of coesite and dolomite in the $4CaMgSi_2O_6 + Ag_2C_2O_4$ starting composition at 6 GPa and 1100 °C indicates that the given parameters correspond to the stability field of Coe + Dol. At 6 GPa, the system began to melt at 1300 °C, where the Coe + Dol (Ca# 42) + L (Ca# 58, 0.7 wt% SiO_2) assemblage appears. The melt Ca# is similar to the peritectic of the $CaCO_3$–$MgCO_3$ system (Shatskiy et al. 2018), which is situated 100 °C higher. The invariant point I_B is located at 4.5 GPa and 1200 °C where Coe, Dol, Cpx, L(C), and F(CO_2) coexist (Figs. 5b-d, 7). At 6 GPa, the melting begins at 1300 °C, where the subsolidus Coe + Dol assemblage coexists with the suprasolidus Coe + L(C) assemblage (Figs. 4a-c, 7). Thus, the coesite-dolomite solidus with a slope of 15 MPa/°C is located at 1200 °C/4.5 GPa and 1300 °C/6 GPa. The position of the invariant point I_B and the solidus line in the range of 4.5-6 GPa differ markedly from those reported by Luth (2006) (Fig. 8). Methods for determining pressure and temperature employed by Luth (2006) are similar to that in the present study. Therefore, the discrepancy due to the difference in the inter-laboratory calibrations of pressure and temperature is unlikely. Alternatively, this discrepancy may be a result of a misinterpretation of the carbonate texture.

From the lower pressure side, the dolomite-coesite field is limited by reaction 2. Following the present results, reaction 2 is situated at 3 GPa and 1000 °C and terminates at an invariant point I_B (Fig. 7). An experimental determination of univariant reaction 2 at 3.0 and 4.5 GPa in the range 950–1200 °C yields an average pressure effect on the equilibrium of 6 MPa/°C (Fig. 7). The established line of reaction 2 has the same Clapeyron slope but is situated 50-90 °C lower as that in the earlier studies (Wyllie et al. 1983; Luth 1995) (Fig. 8).

Comparison of the Ol–Di–CO_2 and Di–CO_2 systems

This is the peer-reviewed, final accepted version for American Mineralogist, published by the Mineralogical Society of America.
The published version is subject to change. Cite as Authors (Year) Title. American Mineralogist, in press.
DOI: https://doi.org/10.2138/am-2022-8588. http://www.minsocam.org/

Above 5 GPa, the solidus of carbonated peridotite and its simple model – the Ol–Di–CO_2 system, is controlled by the reaction of clinopyroxene with magnesite producing orthopyroxene and a carbonate melt (Dalton and Presnall 1998; Shatskiy et al. 2021) (Fig. 9):

$$CaMgSi_2O_6\ (Cpx) + 2MgCO_3\ (Mgs) = Mg_2Si_2O_6\ (Opx) + CaMg(CO_3)_2\ (L). \quad (3)$$

At lower pressure, the Cpx + Mgs assemblage is replaced by Opx + Dol as a result of the Ca-Mg exchange reaction (Brey et al. 1983) (Fig. 9):

$$CaMgSi_2O_6\ (Cpx) + 2MgCO_3\ (Mgs) = Mg_2Si_2O_6\ (Opx) + CaMg(CO_3)_2\ (Dol). \quad (4)$$

The melting of the Opx + Dol assemblage also yields the formation of a carbonate melt (Shatskiy et al. 2021). As the pressure decreases to 2.5 GPa, the Opx + Dol solidus intersects with decarbonation reaction 1, which results in the stabilization of the Ol + Cpx + F(CO_2) assemblage (Fig. 9). The melting of this assemblage occurs at a temperature 400 °C higher than Opx + Dol and is accompanied by the formation of a silicate melt (Eggler and Rosenhauer 1978; Luth 2006).

At 4.5-8 GPa, the solidus of the Di–CO_2 system – a simple model of a mafic suite, is situated ~100 °C lower than that of the ultramafic suite (Fig. 9). The melting is controlled by the Coe + Dol solidus assemblage. The low silica content in the near-solidus melt, ~ 1 wt%, indicates that liquid is produced primarily at the expense of carbonate. The Coe + Dol solidus is located 100 °C below the melting beginning in the $CaCO_3$–$MgCO_3$ system (Shatskiy et al. 2018) revealing the fluxing effect of silica on carbonate melting. The solidus crosses decarbonation reaction 2 at the invariant point I_B situated at 4.5 GPa and 1200 °C (Fig. 9). At lower pressures and higher temperatures, the Cpx + F(CO_2) assemblage becomes stable. The solidus of this assemblage is 350 °C higher than that of Coe + Dol (Fig. 9).

As can be seen in Figure 9, in the presence of CO_2, both the solidus of the ultramafic and mafic systems are characterized by a ledge due to carbonation-decarbonation reactions. To the left of this ledge, at low pressures, CO_2 has a minor fluxing effect, and near-solidus melts have a basaltic

253 composition with dissolved CO_2 (Eggler and Rosenhauer 1978; Luth 2006). To the right of the ledge,
254 at high pressures, the situation changes dramatically. Carbonation reactions stabilize dolomite
255 characterized by low melting temperatures (Shatskiy et al. 2018). This causes a sharp decrease in the
256 solidus temperature of both systems. The resulting melts have a dolomitic composition. The silica
257 content in the near-solidus melt does not exceed 2-4 wt% in the Ol–Di–CO_2 system, and 1 wt% in the
258 system Di–CO_2 (Fig. 10). As temperature increases to 1500 °C at 6 GPa, the melt retains a carbonate
259 composition with 6 and 13 wt% solute SiO_2 in the systems Ol–Di–CO_2 and Di–CO_2, respectively (Fig.
260 10). The near-solidus melts are Ca-rich with Ca# 56 and 58-64 in the Ol–Di–CO_2 and Di–CO_2
261 systems, respectively (Fig. 11). The Ca# of the melt would be controlled by Ca-Mg partitioning with
262 pyroxene and carbonate. The melt Ca# decreases with the increasing temperature approaching the
263 bulk Ca# of the corresponding system (Fig. 11).
264

265 ## Implication

266 The shape of the diopside-CO_2 solidus resembles that of lherzolite solidus in the system CMS–
267 CO_2 (Wyllie and Huang 1975a) but shifted by 2 GPa to higher pressure. Thus, the ledge on the solidus
268 owing to carbonation-decarbonation reactions is a fundamental feature of both ultramafic and mafic
269 systems. At pressure less than 4.5 GPa, corresponding to < 140 km depths, melting of the mafic suite
270 modeled by the CMS–CO_2 system is accompanied by the formation of CO_2-bearing basaltic melts
271 (Luth 2006). The formation of these melts is possible at temperatures exceeding mantle adiabat (Fig.
272 10). Given our results at pressures greater than 4.5 GPa, the Di-CO_2 solidus decreases dramatically,
273 by 350 °C, and melting produces carbonate melt with ≤ 1 wt% SiO_2 (Fig. 10). This melt is stable at
274 depths exceeding 160-170 km along both continental geotherm of 45 mW/m^2 (Hasterok and Chapman
275 2011) and mantle adiabat (Katsura 2022) (Figs. 10). A recent experimental study (Xu et al. 2020)

shows that the presence of carbonate-rich melts in the deep upper mantle is consistent with seismic observations.

On the other hand, the obtained results indicate that the stability field of CO_2 fluid in a mafic suite in the system CMS-CO_2 is limited by pressures below the diamond stability field (Fig. 10). Yet, carbon dioxide inclusions were found in natural diamonds. Schrauder and Navon (1993) reported inclusions of solid carbon dioxide entrapped at depths of about 220-270 km. Tomilenko et al. (2001) described liquid inclusions of CO_2 containing nitrogen and methane in diamonds with a mosaic-block structure belonging to the variety V according to the classification by Yu.L. Orlov (Orlov 1977). Later it was found that these diamonds belong to the eclogitic suite since they contain inclusions of omphacite, pyrope-almandine-grossular garnet, coesite, rutile, and potassium feldspar (Ragozin et al. 2002; Ragozin et al. 2009). Following the classification of Taylor and Neal (1989), the garnets and omphacites from these diamonds belong to eclogite Group C, i.e. garnets are pyrope poor, whereas omphacites are rich in jadeite component (74 mol% jadeite). Temperature estimate assuming pressure 5 GPa based on the garnet-clinopyroxene thermometer (Ellis and Green 1979) corresponds to 1043 °C (Ragozin et al. 2009). Recently, omphacite with similar jadeite content (77 mol%) was obtained in equilibrium with CO_2 fluid in the carbonated pelite system at 6 GPa and 1050 °C (Shatskiy et al. 2019). Thermodynamic analysis of the reaction of CO_2 fluid with eclogite minerals indicates that the jadeite component in clinopyroxene should extend the field stability of clinopyroxene + CO_2 assemblage to lower temperatures (Vinogradova et al. 2021). In this regard, the next goal is to experimentally study the effect of the jadeite component on the phase relationships in the pyroxene-CO_2 system.

Acknowledgments

We are grateful to the anonymous reviewer and Oleg Safonov for reviews and valuable comments, which improved the manuscript. This work is financially supported by Russian Science Foundation (project No 21-17-00024).

References

Brey, G., Brice, W.R., Ellis, D.J., Green, D.H., Harris, K.L., and Ryabchikov, I.D. (1983) Pyroxene-carbonate reactions in the upper mantle. Earth and Planetary Science Letters, 62(1), 63-74.

Buob, A., Luth, R.W., Schmidt, M.W., and Ulmer, P. (2006) Experiments on $CaCO_3$-$MgCO_3$ solid solutions at high pressure and temperature. American Mineralogist, 91(2-3), 435-440.

Dalton, J.A., and Presnall, D.C. (1998) Carbonatitic melts along the solidus of model lherzolite in the system CaO-MgO-Al_2O_3-SiO_2-CO_2 from 3 to 7 GPa. Contributions to Mineralogy and Petrology, 131(2-3), 123-135.

Day, H.W. (2012) A revised diamond-graphite transition curve. American Mineralogist, 97(1), 52-62.

Eggler, D.H., and Rosenhauer, M. (1978) Carbon dioxide in silicate melts; II, Solubilities of CO_2 and H_2O in $CaMgSi_2O_6$ (diopside) liquids and vapors at pressures to 40 kb. American Journal of Science, 278(1), 64-94.

Ellis, D.J., and Green, D.H. (1979) An experimental study of the effect of Ca upon garnet-clinopyroxene Fe-Mg exchange equilibria. Contributions to Mineralogy and Petrology, 71(1), 13-22.

Falloon, T.J., and Green, D.H. (1989) Solidus of carbonated fertile peridotite. Earth and Planetary Science Letters, 94(3-4), 364-370.

Hammouda, T. (2003) High-pressure melting of carbonated eclogite and experimental constraints on carbon recycling and storage in the mantle. Earth and Planetary Science Letters, 214(1-2), 357-368.

Hasterok, D., and Chapman, D.S. (2011) Heat production and geotherms for the continental lithosphere. Earth and Planetary Science Letters, 307(1-2), 59-70.

Hemingway, B.S., Bohlen, S.R., Hankins, W.B., Westrum, E.F., and Kuskov, O.L. (1998) Heat capacity and thermodynamic properties for coesite and jadeite, reexamination of the quartz-coesite equilibrium boundary. American Mineralogist, 83(3-4), 409-418.

Hernlund, J., Leinenweber, K., Locke, D., and Tyburczy, J.A. (2006) A numerical model for steady-state temperature distributions in solid-medium high-pressure cell assemblies. American Mineralogist, 91(2-3), 295-305.

Katsura, T. (2022) A revised adiabatic temperature profile for the mantle. Journal of Geophysical Research: Solid Earth, 127, e2021JB023562.

Lavrent'ev, Y.G., Karmanov, N.S., and Usova, L.V. (2015) Electron probe microanalysis of minerals: Microanalyzer or scanning electron microscope? Russian Geology and Geophysics, 56(8), 1154-1161.

Luth, R.W. (1995) Experimental determination of the reaction dolomite + 2 coesite = diopside + 2 CO_2 to 6 GPa. Contributions to Mineralogy and Petrology, 122(1-2), 152-158.

-. (2001) Experimental determination of the reaction aragonite plus magnesite = dolomite at 5 to 9 GPa. Contributions to Mineralogy and Petrology, 141(2), 222-232.

-. (2006) Experimental study of the $CaMgSi_2O_6$-CO_2 system at 3-8 GPa. Contributions to Mineralogy and Petrology, 151(2), 141-157.

Müller, J., Koch-Müller, M., Rhede, D., Wilke, F.D., and Wirth, R. (2017) Melting relations in the system $CaCO_3$-$MgCO_3$ at 6 GPa. American Mineralogist: Journal of Earth and Planetary Materials, 102(12), 2440-2449.

345 Newbury, D.E., and Ritchie, N.W.M. (2015) Performing elemental microanalysis with high accuracy
346 and high precision by scanning electron microscopy/silicon drift detector energy-dispersive
347 X-ray spectrometry (SEM/SDD-EDS). Journal of materials science, 50(2), 493-518.
348 Newton, R.C., and Sharp, W.E. (1975) Stability of forsterite+CO_2 and its bearing on the role of CO_2
349 in the mantle. Earth and Planetary Science Letters, 26(2), 239-244.
350 Orlov, Y.L. (1977) The Mineralogy of the Diamond. Translated from the Russian edition (Moscow,
351 1973). . John Wiley, New York.
352 Podborodnikov, I.V., Shatskiy, A., Arefiev, A.V., Bekhtenova, A., and Litasov, K.D. (2019) New data
353 on the system Na_2CO_3–$CaCO_3$–$MgCO_3$ at 6 GPa with implications to the composition and
354 stability of carbonatite melts at the base of continental lithosphere. Chemical Geology, 515,
355 50-60.
356 Ragozin, A.L., Shatsky, V.S., Rylov, G.M., and Goryainov, S.V. (2002) Coesite inclusions in rounded
357 diamonds from placers of the Northeastern Siberian Platform. Doklady Earth Sciences, 384(4),
358 385-389.
359 Ragozin, A.L., Shatskii, V.S., and Zedgenizov, D.A. (2009) New data on the growth environment of
360 diamonds of the variety V from placers of the Northeastern Siberian platform. Doklady Earth
361 Sciences, 425(2), 436-440.
362 Schrauder, M., and Navon, O. (1993) Solid carbon dioxide in natural diamond. Nature, 365(6441),
363 42-44.
364 Shatskiy, A., Sharygin, I.S., Gavryushkin, P.N., Litasov, K.D., Borzdov, Y.M., Shcherbakova, A.V.,
365 Higo, Y., Funakoshi, K.-i., Palyanov, Y.N., and Ohtani, E. (2013) The system K_2CO_3-$MgCO_3$
366 at 6 GPa and 900-1450 ºC. American Mineralogist, 98(8-9), 1593-1603.
367 Shatskiy, A., Podborodnikov, I.V., Arefiev, A.V., Litasov, K.D., Chanyshev, A.D., Sharygin, I.S.,
368 Karmanov, N.S., and Ohtani, E. (2017) Effect of alkalis on the reaction of clinopyroxene with

Mg-carbonate at 6 GPa: Implications for partial melting of carbonated lherzolite. American Mineralogist, 102(9), 1934-1946.

Shatskiy, A., Podborodnikov, I.V., Arefiev, A.V., Minin, D.A., Chanyshev, A.D., and Litasov, K.D. (2018) Revision of the $CaCO_3$–$MgCO_3$ phase diagram at 3 and 6 GPa. American Mineralogist, 103(3), 441-452.

Shatskiy, A., Arefiev, A.V., Podborodnikov, I.V., and Litasov, K.D. (2019) Origin of K-rich diamond-forming immiscible melts and CO_2 fluid via partial melting of carbonated pelites at a depth of 180-200 km. Gondwana Research, 75(11), 154-171.

Shatskiy, A., Podborodnikov, I.V., Arefiev, A.V., Bekhtenova, A., Vinogradova, Y.G., Stepanov, K.M., and Litasov, K.D. (2021) Pyroxene-carbonate reactions in the $CaMgSi_2O_6 \pm NaAlSi_2O_6 + MgCO_3 \pm Na_2CO_3 \pm K_2CO_3$ system at 3-6 GPa: Implications for partial melting of carbonated peridotite. Contribution to Mineralogy and Petrology, 176(5), 34.

Shatskiy, A., Bekhtenova, A., Arefiev, A.V., Podborodnikov, I.V., Vinogradova, Y.G., Rezvukhin, D.I., and Litasov, K.D. (2022) Solidus and melting of carbonated phlogopite peridotite at 3-6.5 GPa: Implications for mantle metasomatism. Gondwana Research, 101, 156-174.

Sokol, A.G., Pal'yanov, Y.N., Borzdov, Y.M., Khokhryakov, A.F., and Sobolev, N.V. (1998) Crystallization of diamond from Na_2CO_3 melt. Doklady Akademii Nauk, 361(3), 388-391.

Tappe, S., Foley, S.F., Stracke, A., Romer, R.L., Kjarsgaard, B.A., Heaman, L.M., and Joyce, N. (2007) Craton reactivation on the Labrador Sea margins: $^{40}Ar/^{39}Ar$ age and Sr–Nd–Hf–Pb isotope constraints from alkaline and carbonatite intrusives. Earth and Planetary Science Letters, 256(3-4), 433-454.

Taylor, L.A., and Neal, C.R. (1989) Eclogites with oceanic crustal and mantle signatures from the Bellsbank kimberlite, South Africa, Part I: mineralogy, petrography, and whole rock chemistry. The Journal of Geology, 97(5), 551-567.

393 Tomilenko, A.A., Ragozin, A.L., Shatskii, V.S., and Shebanin, A.P. (2001) Variation in the fluid
394 phase composition in the process of natural diamond crystallization. Doklady Earth Sciences,
395 379(5), 571-574.
396 Vinogradova, Y.G., Shatskiy, A.F., and Litasov, K.D. (2021) Thermodynamic analysis of the
397 reactions of CO_2-fluid with garnets and clinopyroxenes at 3-6 GPa. Geochemistry
398 International, 59(9), 851-857.
399 Wallace, M.E., and Green, D.H. (1988) An experimental determination of primary carbonatite magma
400 composition. Nature, 335(6188), 343-346.
401 Wyllie, P., Huang, W.-L., Otto, J., and Byrnes, A. (1983) Carbonation of peridotites and
402 decarbonation of siliceous dolomites represented in the system CaO-MgO-SiO_2-CO_2 to 30
403 kbar. Tectonophysics, 100(1-3), 359-388.
404 Wyllie, P.J., and Huang, W. (1975a) Peridotite, kimberlite, and carbonatite explained in the system
405 CaO-MgO-SiO_2-CO_2. Geology, 3, 621-624.
406 Wyllie, P.J., and Huang, W.L. (1975b) Inflence of mantle CO_2 ingeneration of carbonatites and
407 kimberlites. Nature, 257(5524), 297-299.
408 Xu, M., Jing, Z., Bajgain, S.K., Mookherjee, M., Van Orman, J.A., Yu, T., and Wang, Y. (2020) High-
409 pressure elastic properties of dolomite melt supporting carbonate-induced melting in deep
410 upper mantle. Proceedings of the National Academy of Sciences, 117(31), 18285-18291.
411
412

Figure captions

Fig. 1. Previous data on phase relations in mafic (black) and ultramafic (green) suits in presence of CO_2, modeled by the CMS-CO_2 system. NS75 – (Newton and Sharp 1975), WH75 – (Wyllie and Huang 1975b), W83 – (Wyllie et al. 1983), B83 – (Brey et al. 1983), H98 – (Hemingway et al. 1998), L95 – (Luth 1995), L06 – (Luth 2006). (Color online)

Fig. 2. Previous experimental data on phase relations in the pyroxene-CO_2 system, established using the oxide-silicate-carbonate starting mixtures: $CaCO_3$+MgO+$2SiO_2$ (Eggler and Rosenhauer 1978; Luth 2006), $CaCO_3$+$MgCO_3$+$2SiO_2$ (Wyllie et al. 1983), and $CaMg(CO_3)_2$+$CaMgSi_2O_6$+$4SiO_2$ (Luth 1995). The numbers denote run durations in hours. Red segments denote the presence of dolomite above its melting temperature established in the $CaCO_3$−$MgCO_3$ system (Buob et al. 2006; Müller et al. 2017; Shatskiy et al. 2018). (Color online)

Fig. 3. BSE images of sample cross-sections from experiment D238 at 6 GPa, 1100 °C, and 147 h with the starting compositions $Ag_2C_2O_4$+$4CaMgS_2O_6$ (a, b) and $CaCO_3$+$MgCO_3$+$2SiO_2$ (c, d) in Pt capsules and $CaCO_3$+$MgCO_3$+$2SiO_2$ in graphite (Gr) capsule (e, f). Color images (b, d, f) were obtained in the element mapping mode. HT – high-temperature and LT – low-temperature capsule ends. The gravity vector is directed downward. The numbers on the upper-right side of each image are the sample numbers. (Color online)

Fig. 4. BSE images of sample cross-sections from experiments at 6 GPa with the $CaCO_3$+$MgCO_3$+$2SiO_2$ starting mixture in graphite capsules: run D225 at 1300 °C with a duration of 21 h (a-c); run D221 at 1400 °C 9 h long (d, e); and run D222 at 1500 °C and a duration of 4 h (f).

HT – high-temperature and LT – low-temperature capsule sides. The gravity vector is directed downward. The numbers on the upper-right side of each image are the sample numbers.

Fig. 5. BSE images of sample cross-sections from experiments at 4.5 GPa with the $CaCO_3$+$MgCO_3$+2SiO_2 starting mixture in graphite capsules: run D234 at 1000 °C with a duration of 115 h (a); run D248 at 1200 °C 25 h long (b-d); and run D219 at 1250 °C and a duration of 24 h (e, f). HT – high-temperature and LT – low-temperature capsule sides. The gravity vector is directed downward. The numbers on the upper-right side of each image are the sample numbers.

Fig. 6. BSE images of sample cross-sections from experiments at 3 GPa in graphite capsules with the starting compositions $Ag_2C_2O_4$+4$CaMgS_2O_6$ (a-d), $CaCO_3$+$MgCO_3$+2SiO_2 (e-j), and $CaCO_3$+$MgCO_3$+SiO_2 (k, l). Run number, temperature, and duration are given above each image. Color images (b, g) were obtained in the element mapping mode. HT – high-temperature and LT – low-temperature capsule sides. The gravity vector is directed downward. The numbers on the upper-right side of each image are the sample numbers. (Color online)

Fig. 7. *P-T* plot illustrating phase relations in the $CaMgSi_2O_6$ + 2CO_2 system. The numbers are run durations in hours. The filled segment of a hexagon denotes the presence of a phase. Color denotes starting material: $CaCO_3$+$MgCO_3$+2SiO_2 is green and 2-3$CaMgSi_2O_6$+$Ag_2C_2O_4$ is blue. The grey segment denotes a minor phase. The melting boundaries for the $CaCO_3$ + MgO + 2SiO_2 starting mixture are from Eggler and Rosenhauer (1978) (circles) and Luth (2006) (triangles). The Arg + Mgs = Dol reaction boundary is from Luth (2001) and that of the Qz-Coe transition from Hemingway et al. (1998). (Color online)

Fig. 8. Comparison of the present and previous data on phase relations in the system $CaMgSi_2O_6$ + $2CO_2$. IR78 – (Eggler and Rosenhauer 1978), W83 – (Wyllie et al. 1983), L95 – (Luth 1995), H98 – (Hemingway et al. 1998), L01 – (Luth 2001), L06 – (Luth 2006). (Color online)

Fig. 9. Comparison of phase relations in mafic (black) and ultramafic (green) suits in presence of CO_2 modeled by the CMS-CO_2 system. (Color online)

Fig. 10. SiO_2 content (wt%) in the melt in the systems Ol–Di–CO_2 (green) (Shatskiy et al. 2017; Shatskiy et al. 2021) and Di–CO_2 (black) (this study). Gr/Dia – graphite-to-diamond transition (Day 2012). Continental geotherms (35, 40, 45 mW/m^2) after Hasterok and Chapman (2011) and rift margin geotherm (~ 60 mW/m^2) after Tappe et al. (2007). (Color online)

Fig. 11. Ca# (mol%) of the melt in the systems Ol–Di–CO_2 (green) (Shatskiy et al. 2017; Shatskiy et al. 2021) and Di–CO_2 (black) (this study). (Color online)

This is the peer-reviewed, final accepted version for American Mineralogist, published by the Mineralogical Society of America.
The published version is subject to change. Cite as Authors (Year) Title. American Mineralogist, in press.
DOI: https://doi.org/10.2138/am-2022-8588. http://www.minsocam.org/

Table 1. Compositions (wt%) of run products at 6 GPa.

Run#	*T*, °C	*t*, h	#	Initial composition	Capsule	Phase	n	SiO_2	MgO	CaO	CO_2(calc)	Total	Ca#	WFP
D238	1100	147	3-3	$Ag_2C_2O_4$+4$CaMgS_2O_6$	Pt	Bulk	–	50.4	16.9	23.5	9.22	100	50	–
						Coe	5	100.2(3)	b.d.l.	b.d.l.	–	100.2(3)	–	13
						Dol	3	b.d.l.	21.9	30.4	47.7	52.1	50	19
						r-Cpx	3	55.8	19.0	26.0	–	100.8	50	68
						Arg(m)	2	b.d.l.	b.d.l.	54.9	45.1	54.9	100	–
						Mgs(m)	5	2.89(16)	46.1(0)	3.46(0)	47.6(1)	52.5(0)	5(0)	–
			4-3	$CaCO_3$+$MgCO_3$+2SiO_2	Pt	Bulk	–	39.5	13.2	18.4	28.9	100	50	–
						Coe	2	100.6	b.d.l.	b.d.l.	–	100.6	–	40
						Dol	5	1.77(95)	21.7(8)	30.6(4)	47.7(8)	53.8(8)	50(1)	61
						Arg(m)	2	0.21	b.d.l.	54.7	45.1	54.9	100	–
						Mgs(m)	1	–	+	+	–	+	–	–
			2-2	–//–	Gr	Coe	5	100.3(3)	b.d.l.	b.d.l.	–	100.3(3)	–	39
						Dol	5	b.d.l.	22.8(0)	29.3(1)	47.9(2)	51.1(1)	48(0)	61
						Arg(m)	1	–	+	+	–	+	–	–
						Mgs(m)	1	–	+	+	–	+	–	–
						Cpx(m)	1	54.7	18.4	23.7	–	97.4	48	–
D225	1300	21	2-2	–//–	Gr	Coe	3	100.1	b.d.l.	b.d.l.	–	100.1	–	39
						Dol	7	b.d.l.	25.9(9)	25.6(5)	48.4(9)	51.58(9)	42(1)	29
						L(C)	5	0.67(7)	17.9(2)	34.6(2)	46.8(3)	55.6(3)	58(0)	32
						Cpx(m)	5	56.7(9)	20.4(5)	23.5(4)	–	100.7(1.6)	45(0)	–
D221	1400	9	2-2	–//–	Gr	Coe	5	99.6(1.0)	b.d.l.	b.d.l.	–	99.6(1.0)	–	35
						Mgs	5	–	38.1(5)	5.78(25)	56.1(3)	43.9(3)	10(1)	5
						L(C)	5	7.09(60)	18.7(4)	30.2(4)	44.1(1.1)	50.4(1.0)	54(0)	60
						Cpx(m)	2	57.7	20.1	19.6	–	97.6	41	–
D222	1500	4	2-2	–//–	Gr	Coe	8	100.6(9)	b.d.l.	b.d.l.	–	100.6(9)	–	31
						L(C)	6	12.9(1.0)	19.1(6)	26.5(4)	41.6(1.9)	59.7(1.9)	50(1)	69

Notes: b.d.l. – below detection limit; m – minor phase; n – number of EDS-SDD analyzes; the numbers in parentheses are standard deviations; WFP – weight fraction of phases estimated using last square method; standard deviations of WFP are < 0.5 wt%; CO_2(Calc) = MgO + CaO.
.

This is the peer-reviewed, final accepted version for American Mineralogist, published by the Mineralogical Society of America.
The published version is subject to change. Cite as Authors (Year) Title. American Mineralogist, in press.
DOI: https://doi.org/10.2138/am-2022-8588. http://www.minsocam.org/

Table 2. Compositions (wt%) of run products at 4.5 GPa.

Run#	*T*, °C	*t*, h	#	Phase		SiO_2	MgO	CaO	CO_2(Calc)	Total	Ca#	WFP
				Bulk	–	39.5	13.2	18.4	28.9	100	50	–
D234	1000	115	2-2	Coe	5	99.5(9)	b.d.l.	b.d.l.	–	99.5(9)	–	40(0)
				Dol	5	0.69(4)	21.7(3)	30.5(3)	47.1(0)	52.9(0)	50(1)	60(0)
				Cpx(m)	3	55.7	18.8	25.4	–	99.9	49	–
D226	1100	35	3-1	Coe	4	99.8	b.d.l.	b.d.l.	–	99.8	–	39(1)
				Dol	7	b.d.l.	23.0(7)	29.1(8)	47.9(8)	52.1(8)	48(1)	61(1)
				Cpx(m)	5	55.7(2)	19.6(2)	25.1(1)	–	100.3(7)	48(0)	–
D233	1100	73	2-2	Coe	4	99.6	b.d.l.	b.d.l.	–	99.6	–	40(0)
				Dol	5	b.d.l.	22.5(2)	29.7(6)	47.8(9)	51.0(9)	49(1)	60(1)
				Cpx(m)	6	55.5(3)	19.3(2)	25.1(2)	–	99.9(6)	48(0)	–
D248	1200	25	4-1	Coe	3	100.5	b.d.l.	b.d.l.	–	100.5	–	11
				Cpx	7	56.0(4)	20.8(3)	23.4(4)	–	100.3(5)	45(1)	51
				Dol	5	b.d.l.	17.3(1)	35.8(3)	46.9(5)	52.7(5)	60(0)	–
				L(C)	5	1.52(48)	15.2(4)	37.3(9)	45.9(9)	50.6(7)	64(0)	17
				CO_2	–	–	–	–	100	100	–	21
D219	1250	24	3-1	Cpx	5	56.2(4)	18.7(1)	25.9(2)	–	100.7(7)	50(0)	71(0)
				CO_2	–	–	–	–	100	100	–	29(0)

Notes: the experiments were carried out using the $CaCO_3$+$MgCO_3$+2SiO_2 starting mixture in graphite capsules; see also Table 1 for other notes.

Table 3. Compositions (wt%) of run products at 3 GPa.

Run#	*T*, °C	*t*, h	#	Initial composition	Phase	n	SiO_2	MgO	CaO	CO_2(calc)	Total	Ca#	WFP
D254	850	169	4-4	$Ag_2C_2O_4$+4$CaMgS_2O_6$	Bulk	–	50.4	16.9	23.5	9.22	100	50	–
					Coe	2	100.1(2)	b.d.l.	b.d.l.	–	100.1(2)	–	11(2)
					Dol	3	b.d.l.	20.8	31.7	47.6	52.3	52	20(1)
					r-Cpx	5	56.2	19.3	24.6	–	100.1	48	69(2)
D312	900	150	2-1	–//–	Coe	2	100.0	b.d.l.	b.d.l.	–	100.0	–	12(2)
					Dol	3	b.d.l.	20.7	31.7	47.5	53.5	52	19(2)
					r-Cpx	6	55.8(4)	19.6(7)	24.4(7)	–	99.7(9)	47(2)	69(3)
D249	1000	118	2-3	–//–	Qz	3	100.2	b.d.l.	b.d.l.	–	100.2	–	3(0)
					Cal	5	b.d.l.	4.34(14)	50.9(2)	44.7	54.8(1)	89(0)	4(0)
					Cpx	7	55.8(6)	19.4(6)	24.8(7)	–	100.1(6)	48(1)	86(0)
					CO_2	–	–	–	–	100	100	–	7(0)
D228	1000	87	2-2	$CaCO_3$+$MgCO_3$+2SiO_2	Bulk	–	39.5	13.2	18.4	28.9	100	50	–
					Qz	5	100.7(9)	b.d.l.	b.d.l.	–	100.7(9)	–	39(0)
					Dol	8	b.d.l.	21.8(4)	30.4(9)	47.7	51.6(1.3)	50(1)	61(0)
					Cpx(m)	7	54.9(0)	19.7(1)	25.1(2)	–	99.7(0)	48(0)	–
					r-Mgs	1	b.d.l.	47.4	0.43	52.1	46.3	1	–
D205	1000	163	3-1	–//–	Qz	5	100.4(5)	b.d.l.	b.d.l.	–	100.4(5)	–	3
					Cal	12	b.d.l.	7.36(26)	47.4(8)	45.24	53.6(4)	82(1)	4
					Cpx	17	55.7(7)	19.5(6)	24.7(4)	–	100.0(1.2)	48(1)	66
					CO_2	–	–	–	–	100	100	–	27
D207	1100	77	3-1	$CaCO_3$+$MgCO_3$+SiO_2	Bulk	–	24.6	16.5	22.9	36.0	100	50	–
					Dol	8	b.d.l.	13.7(1.6)	40.0(2.0)	46.3	52.8(6)	68(4)	39
					Cpx	12	55.8(7)	20.9(6)	22.7(5)	–	99.5(1.1)	44(1)	31
					Opx	3	58.2	37.9	2.25	–	98.3	4	12
					CO_2	–	–	–	–	100	100	–	18

Notes: the experiments were performed in graphite capsules; b.d.l. – below detection limit; m – minor phase; n – number of EDS-SDD analyzes; the numbers in parentheses are standard deviations; WFP – weight fraction of phases estimated using last square method; standard deviations of WFP are < 0.5 wt%; CO_2(Calc) = MgO + CaO.

.

This is the peer-reviewed, final accepted version for American Mineralogist, published by the Mineralogical Society of America.
The published version is subject to change. Cite as Authors (Year) Title. American Mineralogist, in press.
DOI: https://doi.org/10.2138/am-2022-8588. http://www.minsocam.org/

Figure 1

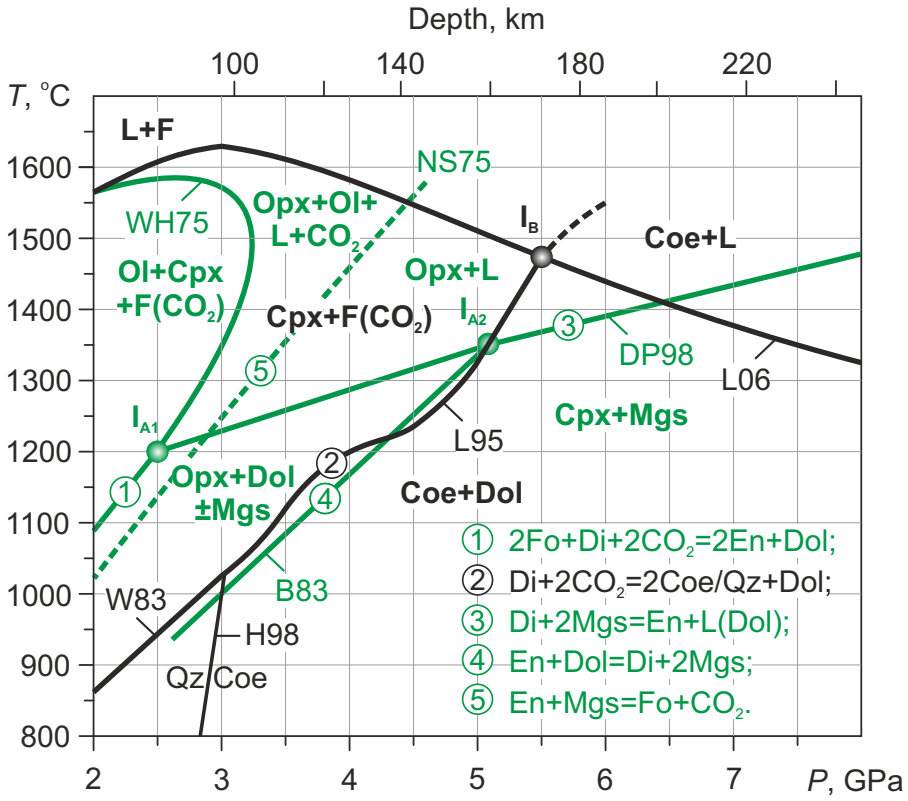

This is the peer-reviewed, final accepted version for American Mineralogist, published by the Mineralogical Society of America.
The published version is subject to change. Cite as Authors (Year) Title. American Mineralogist, in press.
DOI: https://doi.org/10.2138/am-2022-8588. http://www.minsocam.org/

Figure 2

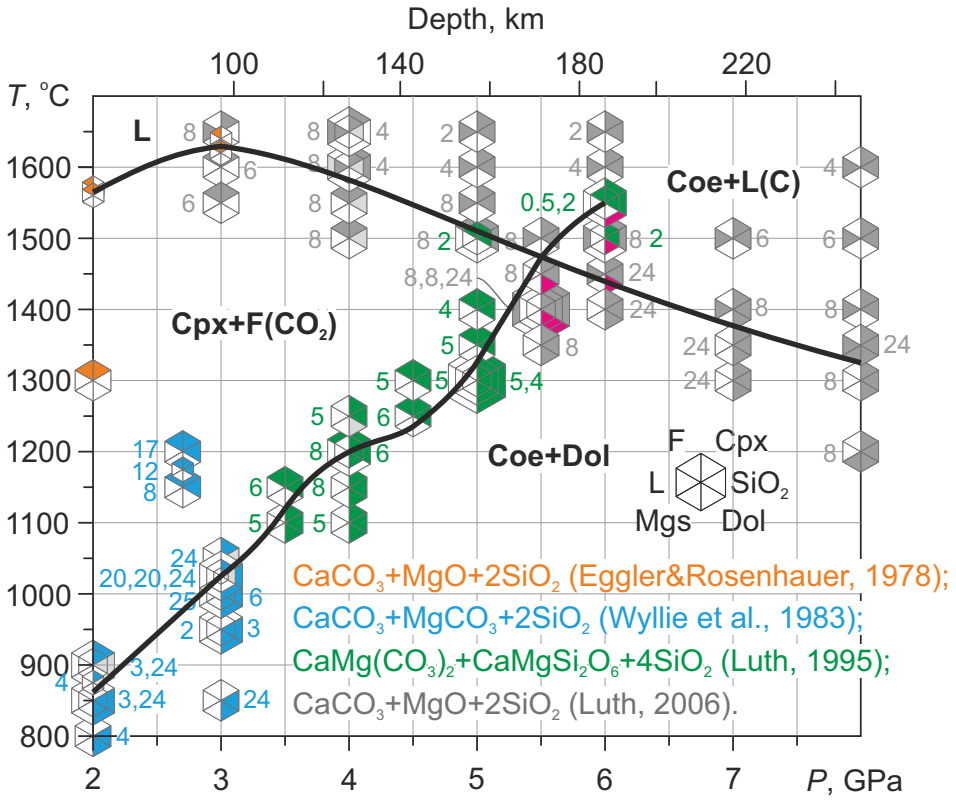

This is the peer-reviewed, final accepted version for American Mineralogist, published by the Mineralogical Society of America.
The published version is subject to change. Cite as Authors (Year) Title. American Mineralogist, in press.
DOI: https://doi.org/10.2138/am-2022-8588. http://www.minsocam.org/

Figure 3

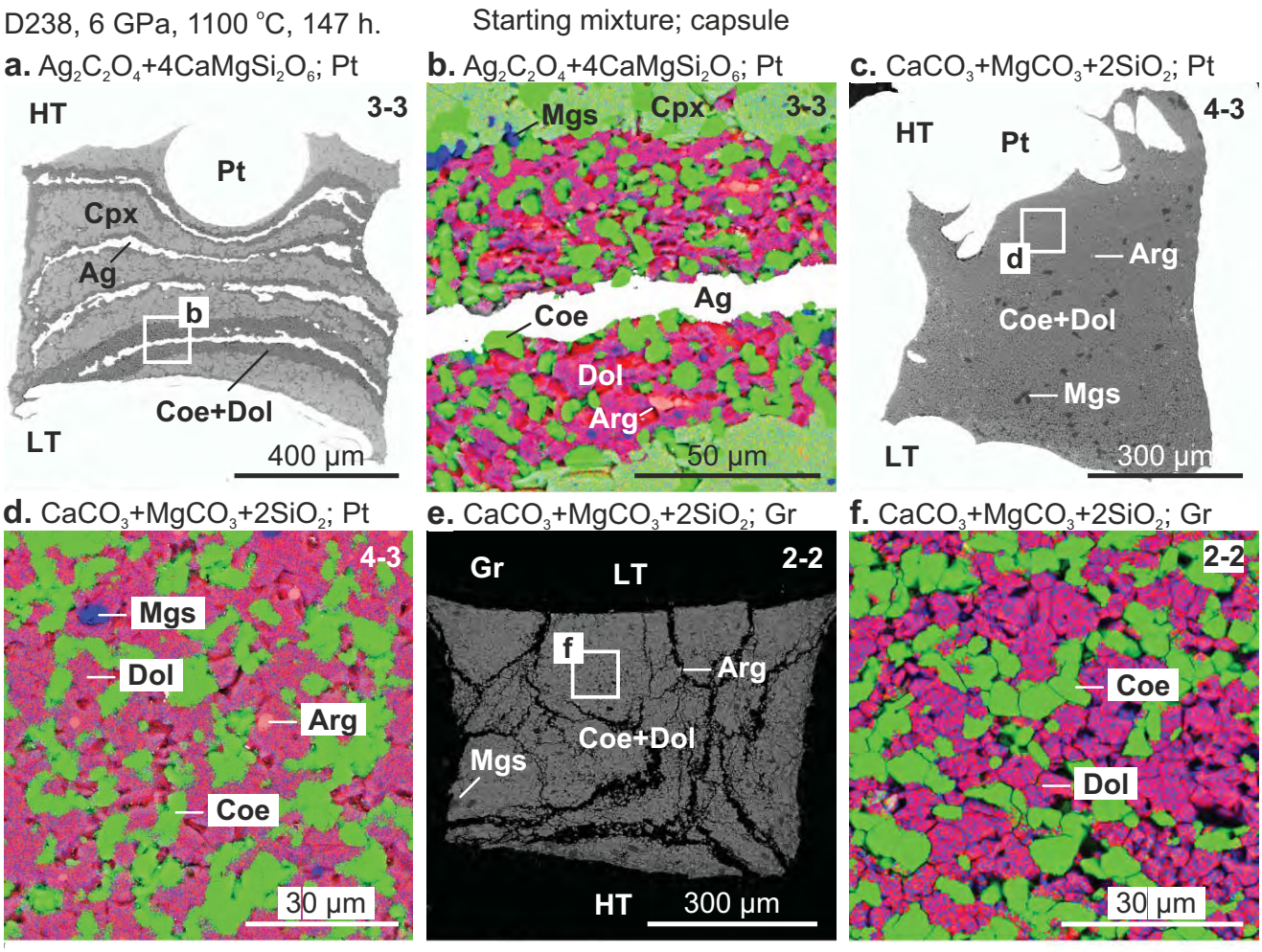

This is the peer-reviewed, final accepted version for American Mineralogist, published by the Mineralogical Society of America.
The published version is subject to change. Cite as Authors (Year) Title. American Mineralogist, in press.
DOI: https://doi.org/10.2138/am-2022-8588. http://www.minsocam.org/

Figure 4

System: $CaCO_3$+$MgCO_3$+2SiO_2.
Pressure: 6 GPa, Gr capsules. Run #; temperature; duration.

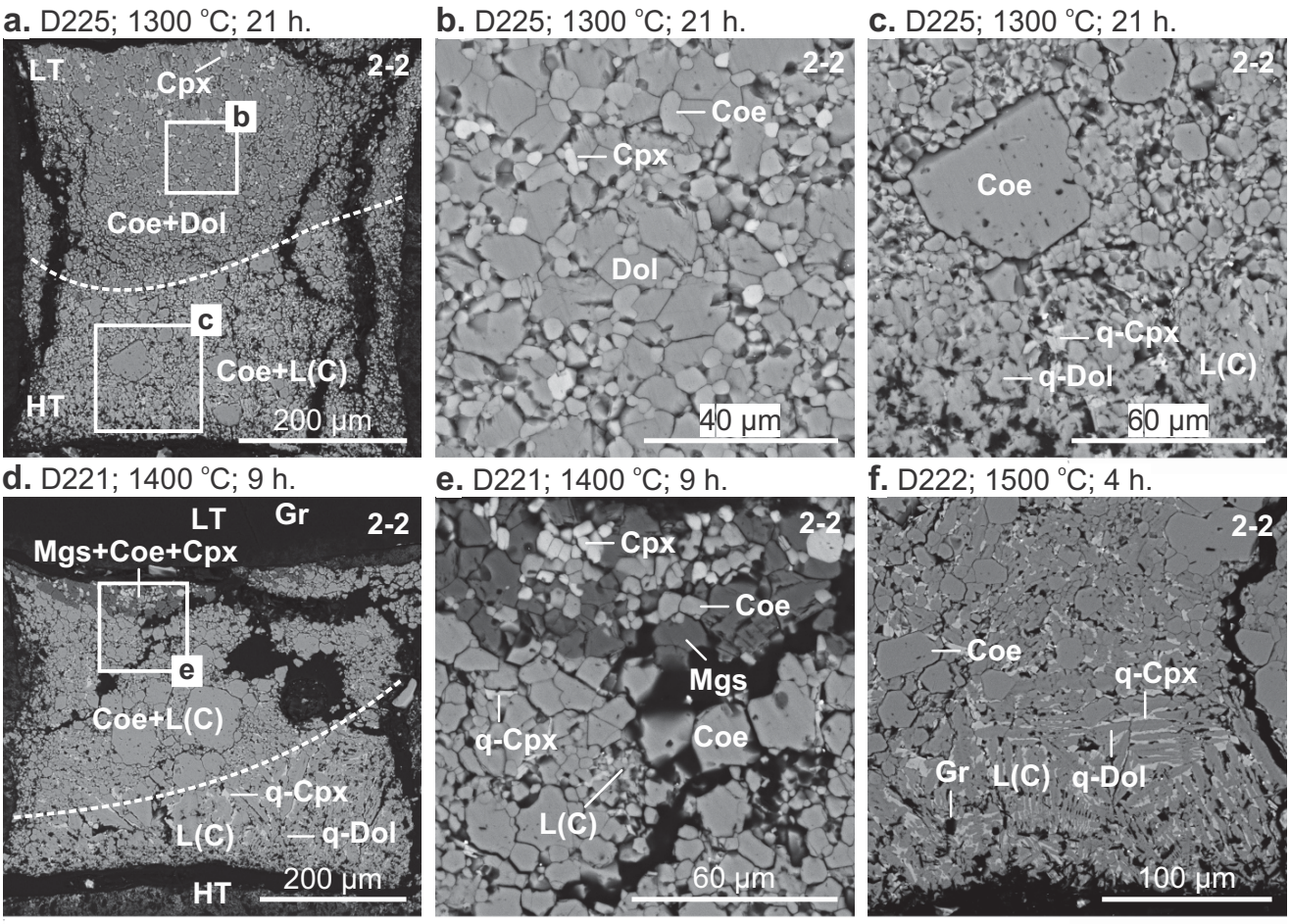

This is the peer-reviewed, final accepted version for American Mineralogist, published by the Mineralogical Society of America.
The published version is subject to change. Cite as Authors (Year) Title. American Mineralogist, in press.
DOI: https://doi.org/10.2138/am-2022-8588. http://www.minsocam.org/

Figure 5

System: $CaCO_3$+$MgCO_3$+2SiO_2.
Pressure: 4.5 GPa, Gr capsules. Run #; temperature; duration.

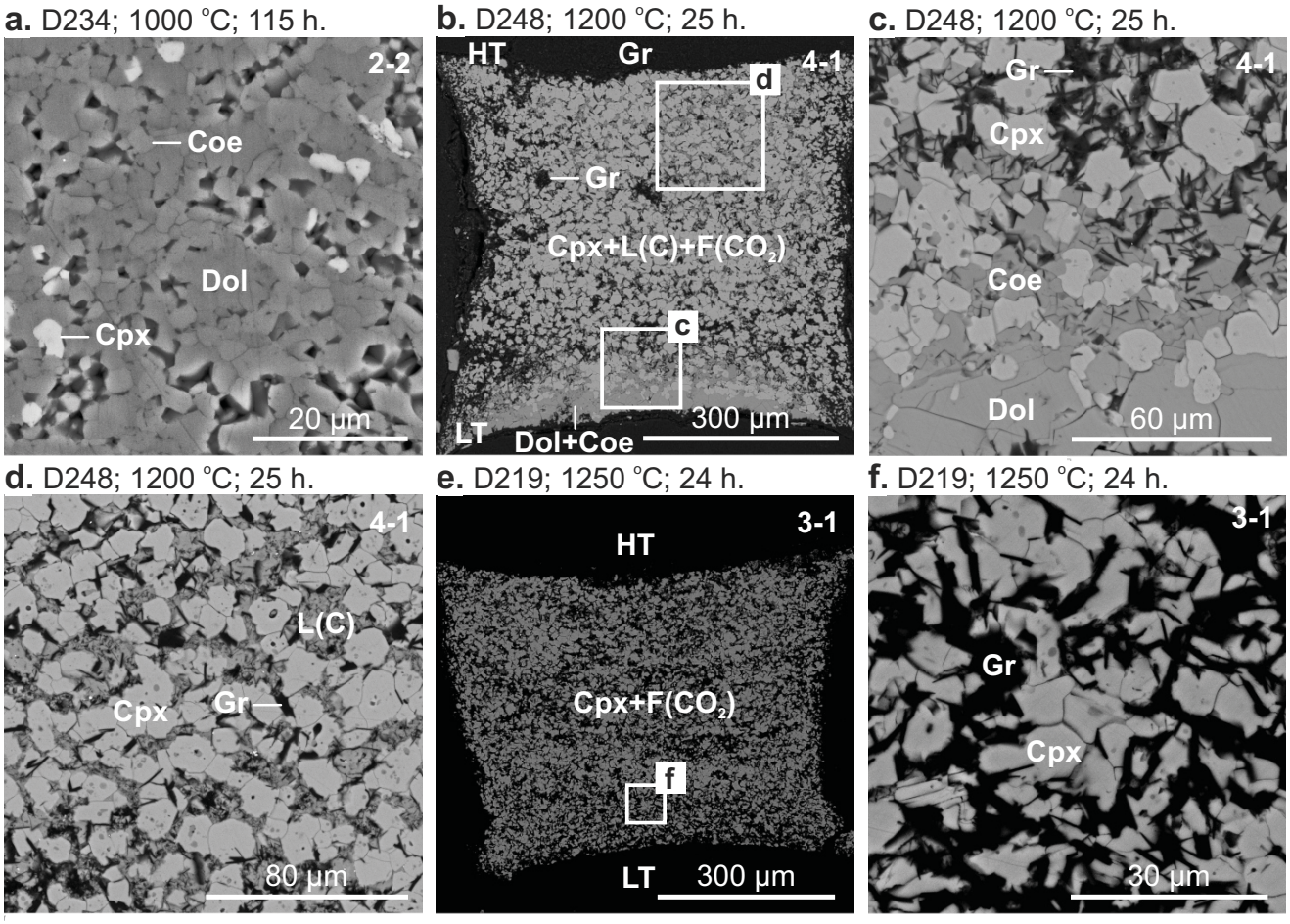

This is the peer-reviewed, final accepted version for American Mineralogist, published by the Mineralogical Society of America.
The published version is subject to change. Cite as Authors (Year) Title. American Mineralogist, in press.
DOI: https://doi.org/10.2138/am-2022-8588. http://www.minsocam.org/

Figure 5

Systems: $Ag_2C_2O_4$+>4$CaMgSi_2O_6$ (a-d), $CaCO_3$+$MgCO_3$+2SiO_2 (e-j), $CaCO_3$+$MgCO_3$+SiO_2 (k-l).
Pressure: 3 GPa, Gr capsules. Run #; temperature; duration.

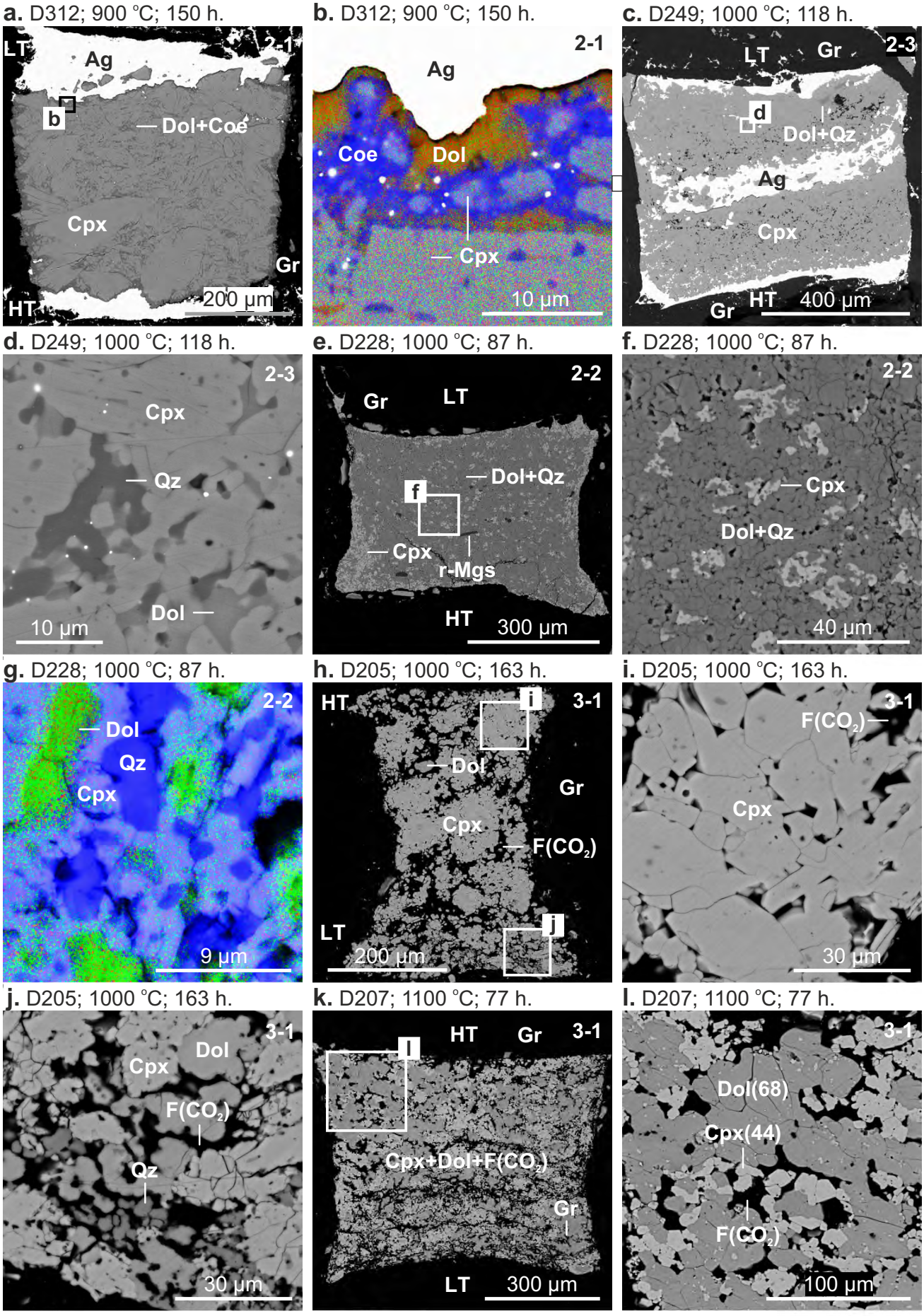

Figure 7

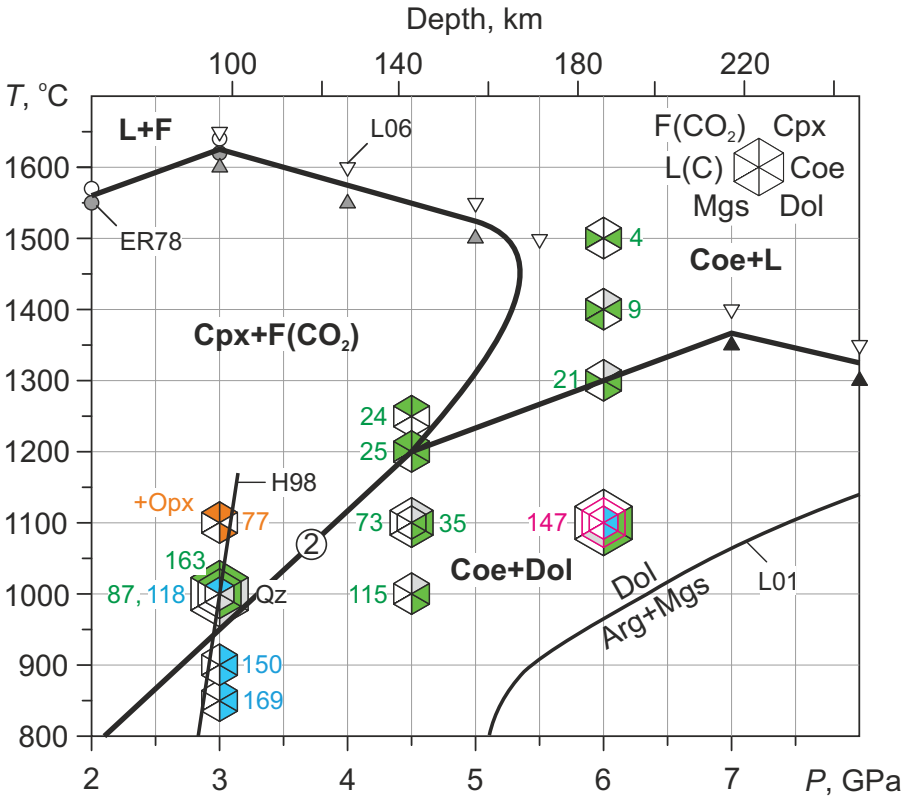

Starting compositions: $CaCO_3+MgCO_3+2SiO_2$ (green),
$Ag_2C_2O_4 + 4CaMgSi_2O_6$ (blue), $CaCO_3+MgCO_3+SiO_2$ (brown).

This is the peer-reviewed, final accepted version for American Mineralogist, published by the Mineralogical Society of America.
The published version is subject to change. Cite as Authors (Year) Title. American Mineralogist, in press.
DOI: https://doi.org/10.2138/am-2022-8588. http://www.minsocam.org/

Figure 8

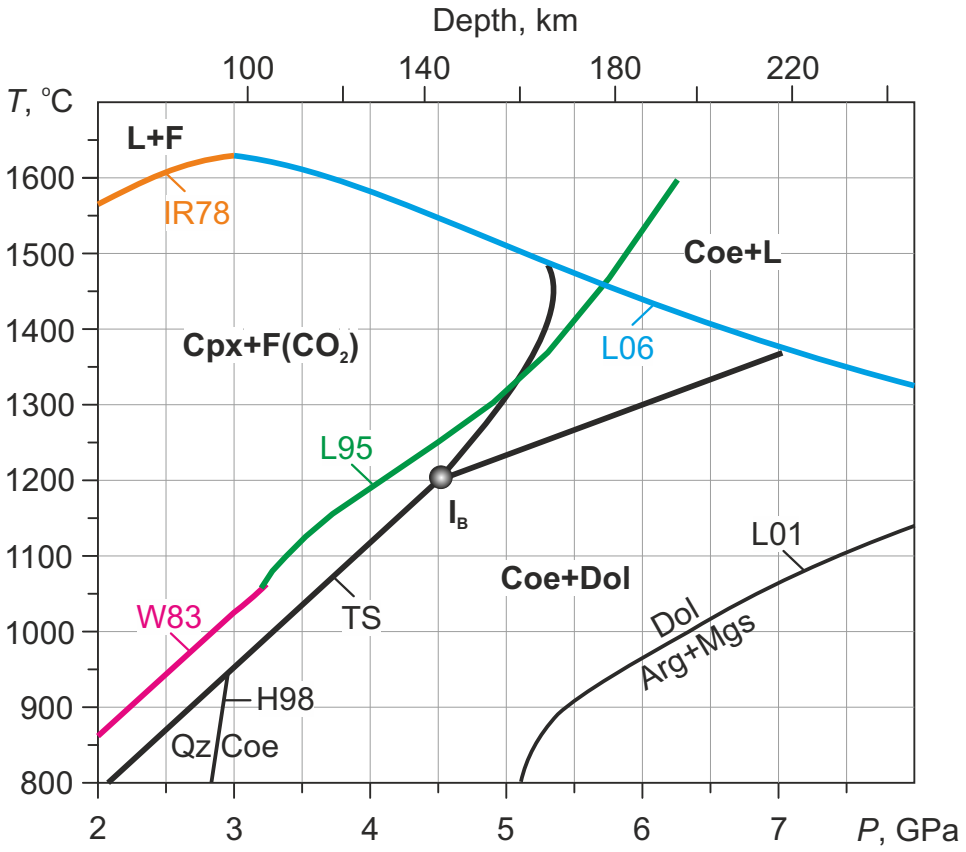

Figure 9

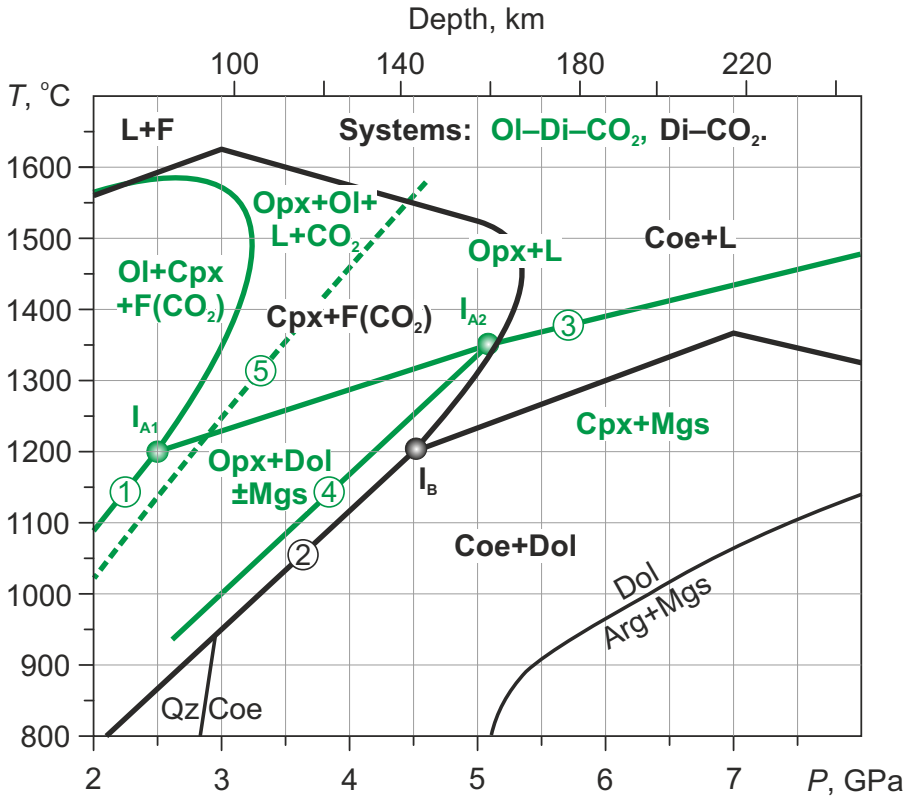

Figure 10

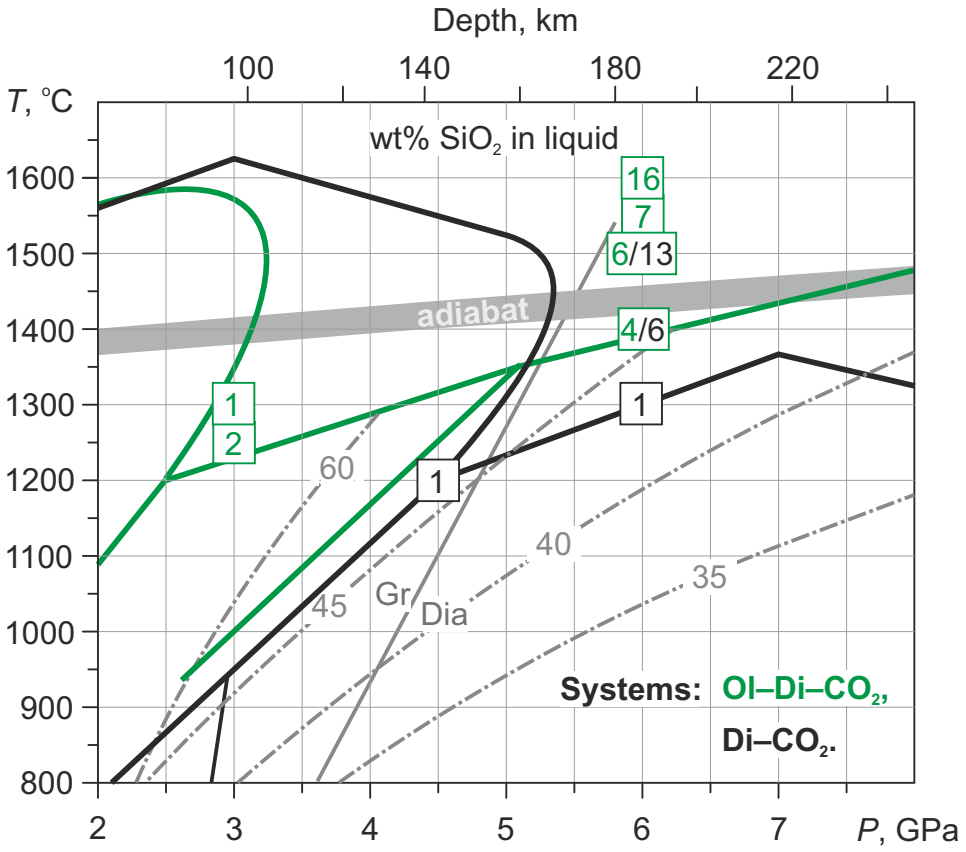

Figure 11